208 *Chem. Mater.* **2011,** *23,* 208–218
DOI:10.1021/cm1026865

CHEMISTRY OF MATERIALS
Article

$LiCo_{1-y}B_yO_2$ As Cathode Materials for Rechargeable Lithium Batteries

C.M. Julien,[†] A. Mauger,*[,‡] H. Groult,[†] X. Zhang,[‡] and F. Gendron[§]

[†]*Laboratoire de Physicochimie des Electrolytes, Colloïdes et Sciences Analytiques, Université Pierre et Marie Curie, Bat. F, 4 place Jussieu, 75005 Paris, France.*, [‡]*Institut de Minéralogie et de Physique des Milieux Condensés, and* [§]*Institut des NanoSciences de Paris, Université Pierre et Marie Curie, 140 rue de Lourmel, 75015 Paris, France*

Received September 17, 2010. Revised Manuscript Received November 25, 2010

Several substituted layered lithium cobaltates of formula $Li_{0.999}Co_{1-y}B_yO_2$ ($0.05 \leq y \leq 0.35$) were synthesized and characterized by X-ray powder diffraction, Raman and FTIR spectroscopy, magnetic measurements, and ESR experiments. The compounds have been investigated as cathode materials in rechargeable lithium batteries and galvanostatic cycling are reported. Structural data showed that particles crystallized in the $R\bar{3}m$ structural symmetry and single-phased can be grown free of any impurity up to the boron concentration $y \leq 0.25$, except for the presence of nickel impurity, as Ni is always present in the cobalt precursors. The voltage profiles of electrochemical cells including these compounds as the cathode were monitored against Li anode. The overall capacity of the oxides has been reduced by the sp metal substitution. However, more stable cycling performances have been observed compared to the performances of the native oxides. At 4.4 V cutoff voltage, the $Li//LiCo_{0.75}B_{0.25}O_2$ cell exhibits an almost constant gravimetric capacity of ca. 127 mA h/g up to the 16th cycle. The origin of the benefit of boron doping is discussed.

1. Introduction

Lithiated layered transition-metal oxides have been considered for application in rechargeable lithium batteries, due to their high concentration of sites available for lithium intercalation, and their high redox potential of the trivalent and tetravalent cations.[1−4] Redox potentials of the first-row transition-metal oxides are highly correlated with the number of d-electrons when they remain within the same space group, and it is possible to tune the voltage by the choice of transition metals in the metal oxide slabs.[5,6]

The most studied cathodes in this series are the $LiMO_2$ with M = Ni and Co.[7,8] These compounds are formed by slabs of MO_2, whereas the lithium ions reside between the slabs to stabilize the structure and compensate the repulsion of the negatively charged MO_2 layers. The cations are octahedrally coordinated with compressed NiO_6 and CoO_6 octahedra and elongated LiO_6 octahedra. According to the $R\bar{3}m$ ($D^5{}_{3d}$) space group, the transition metals are located at the 3*a* sites and the lithium resides at the 3*b* sites. The oxygen anions occupying the 6*c* sites are coordinated with three lithium and three transition-metal ions.

Because of the stronger and more covalent bonding in the CoO_2 slabs, $LiCoO_2$ is less sensitive to synthesis conditions than $LiNiO_2$. Single-phase samples free of any impurity are normally obtained through solid-state reaction of lithium salts and cobalt oxides. The strong covalent bond in $LiCoO_2$, with reduced Co−O bond distance, results in stabilization of Co^{3+} in low-spin ground state, i.e., $d^6 = (t_{2g})^6(e_g)^0$, $S = 0$,[9] and reduces the electronic conductivity of the compound. Strong hybridization with enhanced covalence bonding in MO_2 slabs promotes the long-range order perpendicular to the slab direction. Although the two-dimensional oxides are ideal host structures for ion-electron transfer processes, the amount of lithium that can be inserted and extracted from the layered $Li_{1-x}CoO_2$ compounds without structural degradation is limited to x in the range $1 \leq x \leq 0.5$, and it can be represented by reaction formula

$$(Li_x)_{0.5}(Co^{3+}{}_{0.5}Co^{4+}{}_{0.5})_{3a}(O_2)_{6c} + 0.5Li^+ + 0.5e^- \leftrightarrow LiCoO_2 \quad (1)$$

Deintercalation beyond the reversible limit $x = 0.5$ results in stacking disorder due to a structural transition from rhombohedral to monoclinic phase, as the large change in the *c*-axis might cause a mechanical failure of the material.[10] Recent works have shown that improved

*Corresponding author. E-mail: alain.mauger@impmc.jussieu.fr.

(1) Nagaura, T.; Tozawa, K. *Prog. Batteries Sol. Cells* **1990**, *9*, 209.
(2) Nagaura, T. *Prog. Batteries Mater.* **1991**, *10*, 218.
(3) Thomas, M. G. S. R.; Bruce, P. G.; Goodenough, J. B. *Solid State Ionics* **17, 1985**, 13.
(4) Ohzuku, T.; Ueda, U.; Nagayauna, M. *Electrochim. Acta* **1993**, *38*, 1159.
(5) Ohzuku, T. in Pistoia, G., Eds. *Lithium Batteries*; Elsevier: Amsterdam, 1994; p 239.
(6) Aydinol, M.; K.; Kohan, A. F.; Ceder, G.; Cho, K.; Joannopoulos, J. *Phys. Rev. B* **1997**, *56*, 1354.
(7) Gummow, R. J.; Thackeray, M. M.; David, W. I. F.; Hull, S. *Mater. Res. Bull.* **1992**, *27*, 327.
(8) Broussley, M.; Perton, F.; Biensan, P.; Bodet, J. M.; Labat, J.; Lecerf, A.; Delmas, C.; Rougier, A.; Peres, J. P. *J. Power Sources* **1995**, *54*, 109.
(9) Oku, M. *J. Solid State Chem.* **1978**, *23*, 177.
(10) Reimers, J. N.; Dahn, J. R. *J. Electrochem. Soc.* **1992**, *139*, 2091.

 Published on Web 12/17/2010

cycling stability of $LiCoO_2$ could be achieved by the addition of appropriate dopants (Ni^{3+}, Al^{3+}, Mn^{3+}, etc.), which reduces the volume changes during cycling.[11−15] It is believed that doping effect could prevent the overcharge of the cathode and help to diminish the safety concern regarding the cell operation. As far as we know, there are only two works presenting the use of new cathode materials based on $LiCoO_2$ with boron additives. Alcantara et al.[16] have studied the structure modification of $LiCoO_2$ induced by doping with boron. Galvanostatic cycling of $LiCo_{0.95}B_{0.05}O_2$ revealed that B dopant improves the reversibility of the Li deintercalation-intercalation process and favors lattice adaptation to Li order−disorder in the depleted LiO_2 layers. Nazri et al.[17] have shown that the solubility limit for the formation of solid solution upon substitution of B in $LiCoO_2$ was around 25%. Specific capacities of the $LiCo_{1-y}B_yO_2$ samples were between 120 and 160 mA h/g depending on the amount of substitution.

In this paper, the lithium cobaltates with substitution of B^{3+} for Co^{3+} have been considered as positive electrode materials in rechargeable lithium batteries. The $LiCo_{1-y}B_yO_2$ compounds have been made through solid-state reaction of precursors in an oxygen rich atmosphere. The structural properties of $LiCo_{1-y}B_yO_2$ powders were investigated using X-ray diffraction. Local structure and cationic environment have been probed using Fourier transform infrared spectroscopy. Electrochemical studies were carried out by galvanostatic measurements for the determination of cycling performance.

2. Experimental Section

The $LiCo_{1-y}B_yO_2$ samples were synthesized by direct reaction of LiOH, $LiBO_2$, and Co_3O_4. The homogeneous mixture of the powders was packed in a shallow ceramic boat and heat treated at 450 °C (melting point of LiOH) for 8 h under a flow of oxygen. The products were then ground, packed in the ceramic boats and heat treated at 750 °C for 15 h under oxygen. The last treatment was repeated twice. All powder mixing and grinding were done inside a glovebox under an argon atmosphere to prevent carbonate formation. Loss of lithium compound at high temperature (because of a high volatility of lithium oxide) has been adjusted by adding excess lithium hydroxide (8%). The final composition of each sample was determined by elemental analysis using atomic absorption.

X-ray diffraction (XRD) analysis of samples was made using a diffractometer (Philips model PW 1820) equipped with a diffracted beam graphite single-crystal monochromator and CuK_α radiation source. Data were recorded at a step width and a scan rate of 0.01 and 0.02° per minute, respectively.

Infrared spectra were recorded using Fourier transform infrared (FTIR) spectrometer (Bruker model IFS113v) equipped with a MCT mid-IR, DTGS/PE, and liquid helium cooled far-infrared bolometer detectors. Samples were mixed with KBr or CsI, and pellets were made at 5 tons/cm^2 with good transparency for IR radiation. Data were collected in transmission mode after 128 scans. Raman scattering (RS) spectra of the samples were collected with a double monochromator (Jobin-Yvon model U1000) using the 514.5 nm line from the Spectra-Physics 2020 Ar-ion laser. Raman spectra were recorded using a backscattering geometry, where care has been taken to use a low energy laser beam to prevent reduction of materials by the laser during collection of Raman spectra. The laser power was kept below 25 mW. All spectroscopic data were collected at a spectral resolution of 2 cm^{-1}.

The magnetic measurements (susceptibility and magnetization) were performed with two fully automated SQUID magnetometers (Quantum Design MPMS XL) in the temperature range 4−300 K. Powders were placed into small plastic vial, placed in a holder and finally inserted into the helium cryostat of the SQUID apparatus.

In electron spin resonance (ESR) experiments, the derivative signals of the absorption spectra have been recorded with the use of a X-band VARIAN spectrometer. The powder samples have been placed in an ESR Oxford Instruments continuous flow cryostat, allowing measurements in the whole temperature range between room temperature and 3.5 K. The cryostat itself was inserted in a TE 102 microwave cavity. The frequency of the microwave field was 9.25 GHz. The frequency of the ac modulation magnetic field was 100 kHz, and the dc magnetic field varied in the range 0−2 kOe

Electrochemical measurements were carried out at room temperature (22 °C) with laboratory-scale cells which include a Li metal foil as the counter-electrode, a positive electrode mixture composed of 90 wt % (wt %) of active material, 5 wt % carbon black as a conductive agent, and 5 wt.% polytetrafluoroethylene as a binder. The Li//$LiCo_{1-y}B_yO_2$ cells were housed in a Teflon laboratory-cell hardware employing a nonaqueous Li^+ ion conducting organic electrolyte 1*M* $LiPF_6$ in EC-DMC (1:1). A microporous polypropylene film (Celgard 2500) was used as a separator. To assess the quasi open-circuit voltage profiles, we recorded galvanostatic charge−discharge cycles at a slow scan mode using a Mac-Pile system as follows. A current density of 0.1 mA/cm^2 was supplied for 1 h, corresponding to a lithium extraction of about 0.01 mol from 1 mol of the electrode material. This was followed by a relaxation time of 0.5 h before the next charging started. The charging was stopped when the closed-circuit voltage reached 4.4 V. The apparent lithium content of the charge−discharge compounds was estimated using the current passed and the mass of the electrode material. The data were recorded using a Mac-Pile battery cycler.

3. Results and Discussion

Elemental analysis of samples indicated loss of lithium when heat treatments were made at high temperature (700−800 °C). Usually about 7−10% loss of lithium was observed when the heat treatment was made in a tube furnace under 20 mL/min oxygen flow between 750 and 850 °C for 12 h. The loss of lithium can be adjusted during the preparation of samples by addition of excess lithium compounds (LiOH, Li_2O_2, or Li_2O). The elemental analysis of samples prepared with 8% excess lithium showed formation of stoichiometric compounds. The elemental analysis of each sample was done three times to reduce the

(11) Delmas, C.; Saadoune, I. *Solid State Ionics* **1992**, *53−56*, 370.
(12) Gummow, R. J.; Thackeray, M. M. *J. Electrochem. Soc.* **1993**, *140*, 3365.
(13) Arai, H.; Okada, S.; Sakurai, Y.; Yamaki, J. *J. Electrochem. Soc.* **1997**, *144*, 3117.
(14) Ohzuku, T.; Yanagawa, T.; Kouguchi, M.; Ueda, A. *J. Power Sources* **1997**, *68*, 131.
(15) Jang, Y. I.; Huang, B.; Wang, H.; Sadoway, D. R.; Ceder, G.; Chiang, Y. M.; Liu, H.; Tamura, H. *J. Electrochem. Soc.* **1999**, *146*, 862.
(16) Alcantara, R.; Lavela, P.; Tirado, J. L.; Stoyanova, R.; Zhecheva, E. *J. Solid State Chem.* **1997**, *134*, 265.
(17) Nazri, G. A.; Rougier, A.; Kia, K. F. *Mater. Res. Soc. Symp. Proc.* **1997**, *453*, 635.

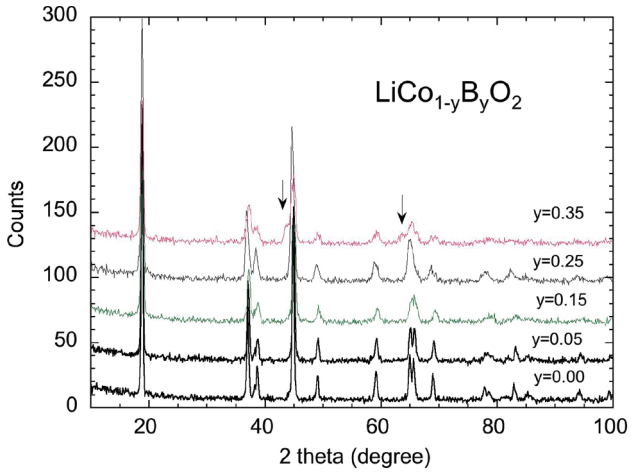

Figure 1. X-ray diffraction patterns of boron substituted $LiCo_{1-y}B_yO_2$ in the composition range $0.05 \leq y \leq 0.35$. An impurity phase at $y \geq 0.25$ is detected by the apparition of additional peaks marked by an arrow.

uncertainty of the results. For all the samples, the composition is Li_xCoO_2 and x is determined within ± 0.002. Adjustment of lithium concentration is thus an important factor for preparation of $LiCoO_2$ free of impurities. A refined value of x will be given by the analysis of the magnetic properties in section 3.3. As we shall see, the final composition of our samples is $Li_{0.999}Co_{1-y}B_yO_2$. Because we are so close to stoichiometry, we still refer to these samples as $LiCo_{1-y}B_yO_2$ for simplicity in the following.

3.1. XRD Diffraction Measurements. Figure 1 displays the XRD patterns of $LiCo_{1-y}B_yO_2$ oxides. These measurements show that the compounds are well crystallized, and that B^{3+} substitutes for Co^{3+} ions in the $LiCoO_2$ rhombohedral structure in the whole composition range $0.05 \leq y \leq 0.35$. The powder XRD patterns of all the samples synthesized for this study could be indexed to the rhombohedral $R\bar{3}m$ space group.[18] With our choice of precursors, no impurity phase was detected in the XRD patterns of $LiCo_{1-y}B_yO_2$ compounds for $y \leq 0.25$. Table 1 shows the lattice parameters of $LiCo_{1-y}B_yO_2$ powders. The a and c lattice parameters were calculated via a least-squares refinement method using 10 well-defined diffraction lines with indexation in the hexagonal system. The lattice parameters for the $LiCo_{1-y}B_yO_2$ materials remain at ca. $a \approx 2.82$ Å and $c \approx 14.02$ Å with $c/a \approx 4.97$. In particular, this constant value of c/a shows that the doping with boron does not increase the trigonal distortion and does not generate any deviation from ideal layered structure. This result suggests that the deformation of the lattice associated with the substitution of Co by B is only local. On another hand, this local deformation generates local strain fields that are responsible for a broadening of the XRD lines. Indeed, as the boron concentration increases, the width of the XRD lines increases, so that the splitting of the (006)(102) and (108)(110) Bragg lines could be observed only for $y < 0.15$. This is not surprising since boron tends to bond to oxygen in tri- or tetra-coordination, which generates a strain adding to the microscopic strain in the unit cell

(18) Orman, H. J.; Wiseman, P. J. *Acta Crystallogr., Sect. C* **1984**, *40*, 12.

Table 1. XRD Parameters for $LiCo_{1-y}B_yO_2$ Materials

y boron	a (Å)a	c (Å)[a]	c/a	V (Å^3)
0.05	2.8230(5)	14.021(6)	4.967	96.80
0.15	2.8222(1)	14.038(3)	4.974	96.83
0.25	2.8210(1)	14.022(1)	4.970	96.70
0.35	2.8223(4)	14.022(7)	4.968	96.49

[a] Lattice constants a and c were calculated via a least squares refinement program.

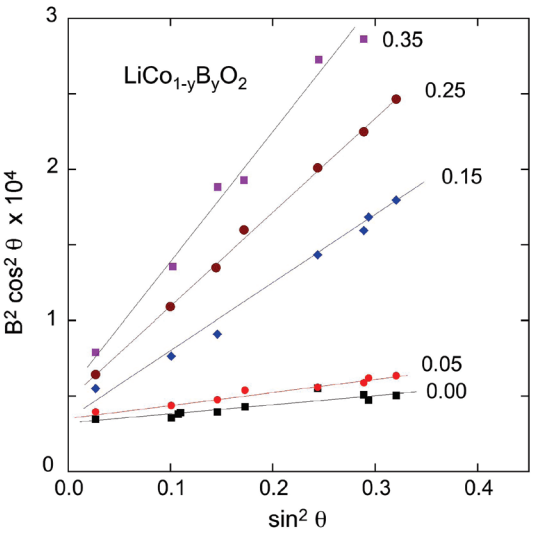

Figure 2. Analysis of the full-width B at half-maximum of the XRD peaks according to eq 2. B is in radians.

due to B^{3+} for Co^{3+} ions. This strain is responsible for a broadening of Bragg peaks for $LiCo_{0.65}B_{0.35}O_2$ powders. The profile of the Bragg lines is thus the combination of the Scherrer's equation for crystallite size and the Bragg's law for diffraction, according to the equation

$$B^2\cos^2\theta = 16\langle e^2\rangle \sin^2\theta + \frac{K^2\lambda^2}{L^2} \qquad (2)$$

where B is the full-width at half-maximum (fwhm) in radian, θ is the diffraction angle and K is a near-unity constant related to crystallite shape. The crystallite size L and microstrain local $\langle e^2\rangle$ are determined by using this equation. The plot of the first member as a function of $\sin^2\theta$ is reported in Figure 2 for different boron concentrations. The plots are well-fit by straight lines, in agreement with eq 2. Note this linearity also gives indirect evidence that L is independent of the wave vector q. The crystallites are then spherical in first approximation, so that we take for the constant K the value appropriate to this particular case $K = 0.9$. The slope of the linear fit of the data provides us with the value of $\langle e^2\rangle$, whereas the extrapolation to $\sin\theta = 0$ provides us with the value of the coherence length L. Indeed, the strain $[\langle e^2\rangle]^{1/2}$ increases importantly with y, as shown in Figure 3. On another hand, we find that $20 \leq L \leq 25$ nm for all the samples in the range $y \leq 0.25$, so that the addition of boron does not significantly affect the coherence length. This is another evidence that the $LiCoO_2$ framework and the layered structure is well preserved upon the incorporation of the boron up to $y = 0.25$. Further information can be obtained from the

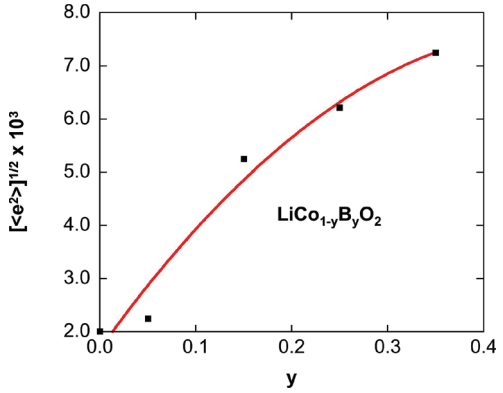

Figure 3. Strain field (see eq 2) as a function of y in $LiCo_{1-y}B_yO_2$. The symbols are experimental, the line is only a guide for the eyes.

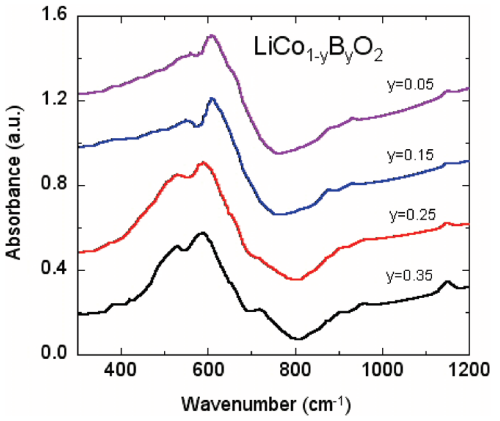

Figure 4. FTIR spectra of $LiCo_{1-y}B_yO_2$ layered materials at various levels of B substitution ($0.05 \leq y \leq 0.35$).

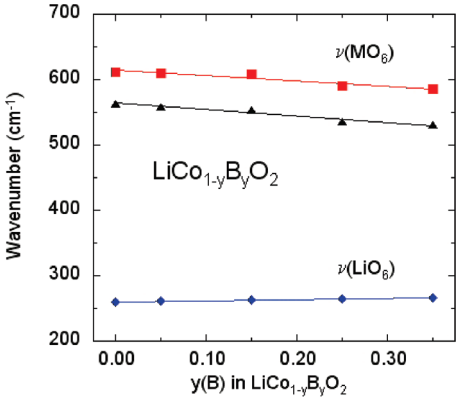

Figure 5. Frequency of the IR modes as a function of the boron concentration in $LiCo_{1-y}B_yO_2$.

intensity ratios of I_{104}/I_{003} and $I_{(006+102)}/I_{101}$. The cation ordering normally decreases the value of these ratios. Our results are thus consistent with an enhancement of the cation ordering resulting from the large difference between ionic radii of B^{3+} (41 pm) and Co^{3+} (68 pm).[19]

For the highest concentration of B dopant ($y = 0.35$), the XRD intensity ratios are affected by B concentration and the hexagonal unit cell volume is also modified. In addition, any attempt of doping at concentration $y > 0.25$ generates impurity phase in the sample detected by XRD (Figure 1), so that $y = 0.25$ can be considered as the limit of solubility of the boron in $LiCoO_2$, in agreement with the result of ref 17. Note, however, that this limit is much higher than the 5% reported in ref 16. This difference is presumably due to the different choice of precursor. In ref 16, the precursor for boron was H_3BO_3; in our case, it is $LiBO_2$, which is more appropriate because it avoids the BO_3 rings. There are two possibilities for the location of boron atoms into the $LiCoO_2$ lattice. If a substitution of small boron ions for cobalt ions is present, the unit cell should shrink because of the 3*a* site occupancy in the CoO_2 layers. On the contrary, if the B atoms are located in crystallographic sites different from those used by the constituent atoms in stoichiometric $LiCoO_2$, i.e., pseudo-tetrahedral 6*c* sites, no reduction in cell volume is expected. As shown in Table 1, this second hypothesis holds true for $LiCo_{1-y}B_yO_2$, in agreement with the result of Alcantara et al.[16] These structural aspects will be reconsidered in the next section.

3.2. Vibrational Spectra. The FTIR spectra of the lithium cobaltates doped with various amounts of boron are shown in Figure 4. Materials with layered structure and crystallographic $R\bar{3}m$ space group have a corresponding spectroscopic space group of D^5_{3d}.[20] The factor group analysis of D^5_{3d} yields four IR active ($2A_{2u}+2E_u$) and two Raman ($A_{1g}+E_g$) active vibration modes. The A_{1g} and E_g Raman active modes, which correspond mainly to vibrations of oxygen cages, i.e., O−O vibrations in the *c* direction and in parallel to the Li and transition metal planes, are located in the range 400−650 cm^{-1}. The position of these bands are less sensitive to the transition metals, but their intensities are very sensitive to the long-range order in MO_2 slabs.[20,21]

The pure $LiCoO_2$ phase has two high-frequency infrared peaks situated at 595 and 515 cm^{-1}, which are characteristic of the CoO_6 vibrations.[22,23] Substitution of cobalt for boron reduces the resolution of the two peaks and induces a frequency shift as shown in Figure 5. The systematic shift in band frequency as a function of boron concentration is expected for all the bands, and has been observed.[24] However, we find that the lower-frequency IR peak located at 515 cm^{-1} is more sensitive to the addition of boron. Both the frequency shift of CoO_2 vibrations and the broadening of the high-frequency bands are due to the presence of B atoms, as a result of the increase in CoO_6 distortion upon the introduction of boron. This feature implies that the boron is located in the CoO_2 layers. As is evident from Figure 4, another band is detected, the intensity of which does not significantly depend on the concentration in boron, at 660 cm^{-1}. This band has been attributed to a residual concentration of Co^{3+} ions located in the lithium

(19) Shannon, R. D.; Prewitt, C. T. *Acta Crystallogr., Sect. B* **1989**, *25*, 925.
(20) Moore, R. K.; White, W. B. *J. Am. Ceram. Soc.* **1970**, *53*, 679.
(21) Inaba, M.; Todzuka, Y.; Yoshida, H.; Grincourt, Y.; Tasaka, A.; Tomida, Y.; Ogumi, Z. *Chem. Lett.* **1995**, *24*, 88.
(22) Julien, C. M.; Rougier, A.; Nazri, G. A. *Mater. Res. Soc. Symp. Proc.* **1997**, *453*, 647.
(23) Julien, C. M.; Michael, S. S.; Ziolkiewicz, S. *Intl. J. Inorg. Mater.* **1999**, *1*, 29.
(24) Chang, I. F.; Mitra, S. S. *Phys. Rev.* **1968**, *172*, 924.

layer in the lithium ions sites.[25] This exchange of position between Li^+ and Co^{3+} is always met in layer compounds, and it can affect up to 6% of the Co^{3+} ions in $LiCoO_2$ prepared at low temperature.[26] In the present case, however, the samples have been synthesized at high temperature, and the mixing is much smaller, but still detectable by FTIR, like in prior works.[25] Five new infrared bands appear upon boron substitution, located at 340, 720, 875, 925, and 1150 cm^{-1}. A detailed interpretation of the IR spectra of borate components is not an easy task, due to the complexity originating from the large number of possible structural groups found in borate glasses.[27] However, it is generally accepted that the broad absorption region 1200−1450 cm^{-1} corresponds to B−O bond stretching of trigonal BO_3 units, while that in the region 850−1100 cm^{-1} originates from B−O bond stretching of tetrahedral BO_4 groups. The band at 720 cm^{-1} is assigned to bond-bending vibrations of B−O−B linkages in the boron−oxygen network.

Note the intensity of the bands associated with boron have grown up importantly in the $y = 0.35$ sample. This result suggests that, for such a large value of y, the boron may form nanoclusters of impurities involving the pyroborate group (B_2O_5) and/or the metaborate group (BO_3), again pointing out that this boron concentration exceeds the limit of solubility. It is well-known that boron oxide is used as glass former, and it may reduce the long-range order in the $LiCoO_2$ lattice by generating such nanoscaled or molecular-scaled clusters. This effect is also seen in X-ray diffraction of lithium cobaltates doped with boron. The IR vibration modes of the LiO_6 octahedra appear in far-infrared region, at ca. 250 cm^{-1}. As the boron substitution does not strongly affect the far-infrared region (Figure 5), the LiO_2 layers retain similar structure, which is suitable for deintercalation-intercalation reaction in the cathode materials. The Raman spectra of the above materials are examined next, to confirm these trends.

Figure 6 shows the RS spectra of $LiCo_{1-y}B_yO_2$ ($0.05 \leq y \leq 0.35$) layered materials. The two predicted Raman-active modes of $LiCoO_2$ are located at 485 and 595 cm^{-1}, which are in good agreement with the factor group analysis of the $R\bar{3}m$ symmetry. They are attributed to the Raman-active species E_g and A_{1g}, respectively.[21] The Raman bands are associated with the motions involving mainly the Co−O stretching and O−Co−O bending. The A_{1g} mode has the greater oscillator strength and exhibits an intensity twice that the c mode. Note the contributions to these Raman modes only come from the motion of oxygen atoms. This is the reason why these Raman bands are not sensitive to the doping with boron, at contrast with the FTIR bands that are related to the motion of cobalt (or boron). On another hand, the appearance of new bands at 984 and 1170 cm^{-1} in the Raman spectra are attributed to the stretching modes of BO_3 units (orthoborate groups). For

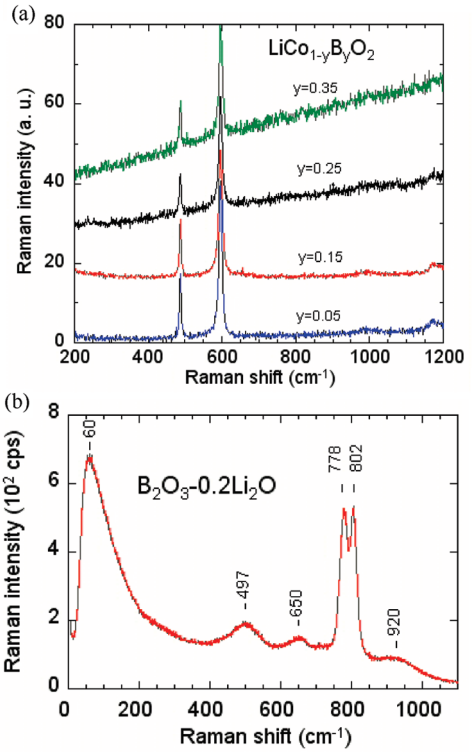

Figure 6. Raman scattering spectra of (a) $LiCo_{1-y}B_yO_2$ layered materials at various levels of B substitution ($0.05 \leq y \leq 0.35$) and (b) lithium borate $B_2O_3-Li_2O$ for comparison.

$y \geq 0.25$, a strong background signal appears in the high-frequency side. This feature is a luminescence band attributed to the creation of a donor level with the incorporation of boron in the $LiCoO_2$ framework, which is again the signature that the solubility limit is $y = 0.25$. In the light of the above results, we can now focus on a reasonable explanation for the site occupancy of tricoordinated boron dopants.

3.3. Magnetic Properties. The magnetic properties are the most sensitive tool to characterize impurities and defects in cathode elements.[28] For the particular case of Li_xCoO_2, this magnetic characterization has been performed in several works[29−31] (without boron doping). The magnetization curves $M(H)$ obtained on our samples are illustrated for the case $y = 0.25$ in Figure 7. The magnetization curves are not linear in H at small field, which is evidence of the existence of small ferromagnetic clusters. The magnetization in this case is just the addition of the contribution of this impurity, which saturates easily in field to a value M_s, and the intrinsic part that is linear in H. Following the procedure described in prior works,[32,33] we determine M_s by the intercept of the linear law $M(H)$

(25) Rao, K. J.; Benqlilou-Moudden, H.; Desbat, B.; Vinatier, P.; Levasseur, A. *J. Solid State Chem.* **2002**, *165*, 42.
(26) Gummov, R. J.; Lilies, D. C.; Tackeray, M. M.; David, W. I. F. *Mater. Res. Bull.* **1993**, *27*, 1177.
(27) Kamitsos, E. I.; Karakassides, M. A.; Chryssikos, G. D. *Phys. Chem. Glasses* **1987**, *28*, 203.
(28) Julien, C. M.; Mauger, A.; Ait-Salah, A.; Massot, M.; Gendron, F.; Zaghib, K. *Ionics* **2007**, *13*, 395.
(29) Imanishi, N.; Fujiyoshi, M.; Takeda, Y.; Yamamoto, O.; Tabuchi, M. *Solid State Ionics* **1999**, *118*, 121.
(30) Hertz, J. T.; Huang, Q.; Mc Queen, T.; Klimczuk, T.; Bos, J. W. G.; Viciu, L.; Cava, R. J. *Phys. Rev. B* **2008**, *77*, 075119.
(31) Kellerman, D. G.; Galakhov, V. R.; Semenova, A. S.; Blinovskov, Ya. N.; Leonidova, O. N. *Phys. Solid State* **2006**, *48*, 548.
(32) Ait-Salah, A.; Mauger, A.; Julien, C. M.; Gendron, F. *Mater. Sci. Eng., B* **2006**, *129*, 232.
(33) Julien, C. M.; Mauger, A.; Ait-Salah, A.; Massot, M.; Gendron, F.; Zaghib, K. *Ionics* **2007**, *13*, 395.

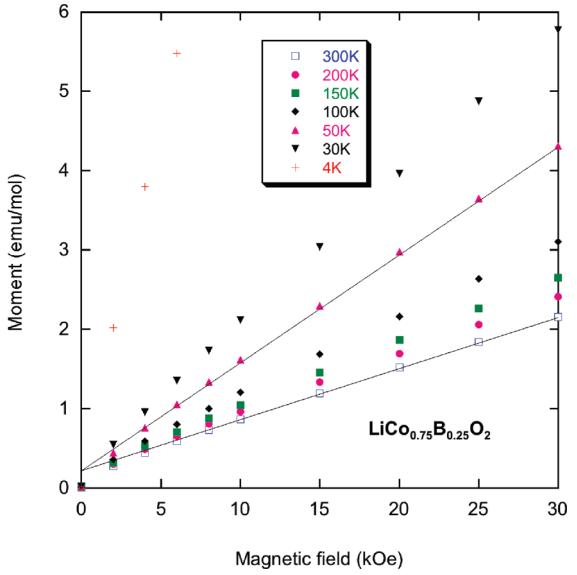

Figure 7. Magnetization curves for the sample $LiCo_{0.25}B_{0.75}O_2$. The straight lines are the intrinsic components (drawn at two temperatures only for clarity). Their extrapolation to $H = 0$ gives the magnetic moment M_s associated with nickel (in concentration 60 ppm) that has precipitated under the form of ferromagnetic nanoparticles.

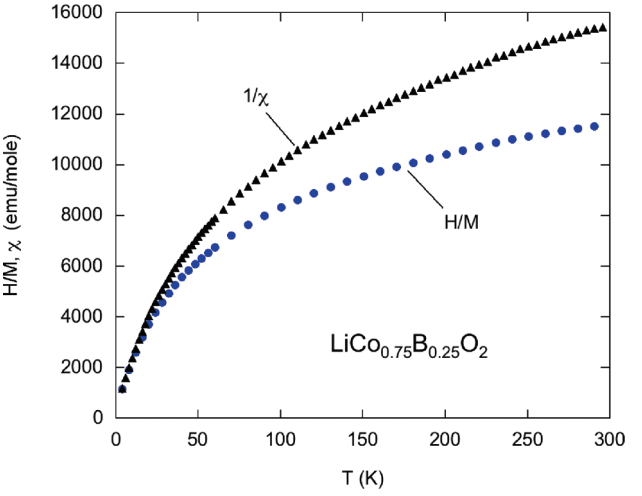

Figure 8. Plot of the inverse of the magnetic susceptibility as a function of temperature. Only half of the experimental data H/M measured in $H = 10$ kOe have been reported for clarity (circles). The triangle symbols are obtained after subtraction of the spurious contribution of ferromagnetic cobalt clusters: $\chi^{-1} = H/(M-M_s)$, where M_s is defined in Figure 7.

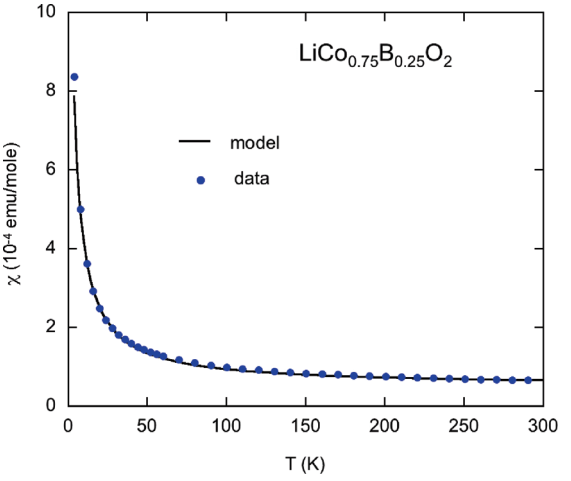

Figure 9. Magnetic susceptibility $\chi(T)$ defined in Figure 7, and theoretical fit (eq 2 in the text) for $LiCo_{0.25}B_{0.75}O_2$.

at $H > 10$ kOe with the ordinate axis $H = 0$. Because the value of M_s does not depend on temperature, the Curie temperature of the impurity phase is much larger than room temperature; the first idea is to identify this impurity as metallic cobalt. In its most stable (hexagonal) phase, the magnetic moment of bulk cobalt is 1.7 μ_B per Co atom. Therefore, the value $M_s = 0.22$ emu per mole of product in the $y = 0.25$ sample would correspond to a concentration 23×10^{-6} (i.e., 26 ppm) of cobalt that has precipitated. The same analysis for the other samples would lead to 30 ppm for the $y = 0.15$ sample, 60 ppm for $y = 0.05$. However, ESR experiments reported in the next section will give some evidence that the origin of this extrinsic ferromagnetic component to the magnetization is actually due to Ni nanoparticles. The cobalt salts usually contain a small concentration (<0.4%) of Ni impurities, due to the recurrent presence of Ni in the commercial cobalt used for the preparation of the samples. In the present case, part of this nickel has precipitated to form ferromagnetic nanoparticles. Because the magnetic moment of bulk nickel is 0.6 μ_B per Ni atom, the concentration of nickel involved in the particles of nickel is 65 ppm for the $y = 0.25$ sample, and 85 170 ppm for the $y = 0.15$ and 0.05 samples, respectively.

The parasitic contribution to the magnetization associated with the presence of nearly 0.01% Ni that has precipitated under the form of Ni nanoparticles must be taken into account to analyze the magnetic properties. This is best evidenced in Figure 8, in which we have reported both the rough experimental data H/M measured at $H = 10$ kOe with the SQUID magnetometer, and the inverse of the intrinsic susceptibility, defined as $\chi = (M - M_s)/H$ as a function of the temperature T for the same sample $y = 0.25$. This figure also shows that χ^{-1} is not linear in T, so that the Curie−Weiss law is not satisfied. Like in prior works, we then have to analyze the results with the modified Curie−Weiss law

$$\chi = \chi_0 + C/(T+\theta) \qquad (3)$$

The fit is shown in Figure 9. We find $\chi_0 = +5 \times 10^{-5}$ emu/mol for this sample. This value is positive. This is in agreement with the prior works that usually report that $LiCoO_2$ is paramagnetic, although this feature has not been discussed so far in this compound. Co^{3+} is known to be in the low spin state $S = 0$. We have investigated the electronic structure and the related magnetic properties of the d^6 shell of Co^{3+} and Fe^{2+} ions in the low spin state in prior works.[34,35] As a result, these are Van-Vleck ions, with a Van-Vleck paramagnetic contribution χ_p that is larger than the diamagnetic one χ_d, so that $\chi_0 = \chi_p + \chi_d$ is

(34) Mauger, A.; Scalbert, D.; Gaj, J.; Benoit à la Guillaume, C. *Phys. Rev. B* **1991**, *43*, 7102.
(35) Mycielski, A.; Arciszewska, M.; Dobrowolski, W.; Lusakowski, A.; Dybko, K.; Szymczak, R.; Szadkowski, A. *Phys. Rev. B* **1995**, *53*, 10732.

positive. In the cubic crystal-field environment, the term χ_p is temperature independent, and is associated with the coupling between the nondegenerate (i.e., nonmagnetic) ground state and the magnetic excited state of these ions by the spin−orbit operator. χ_p is thus the unquenched orbital moment contribution to the magnetic susceptibility. The resulting positive and temperature independent χ_0 has been observed for instance in CoO where the cobalt is in the Co^{2+} configuration[36,37] and in Co_3O_4 which is a mixture of Co^{3+} and Co^{2+} ions.[38] Closer to the material investigated here, the orbital contribution χ_p has been estimated in $Na_{1-x}CoO_2$[39] where Co is trivalent. The result in this case is $\chi_p = 15 \times 10^{-5}$ emu/mol, and the diamagnetic contribution is about 3.5×10^{-5} emu/mol. In our samples, we find $\chi_0 = 6 \times 10^{-5}$ emu/mol in the $y = 0.05$ case. This value is consistent with the value $\chi_0 = 5 \times 10^{-5}$ in the $y = 0.25$ sample (against 6×10^{-5} emu/mol in the $y = 0.05$ case), taking into account the difference in the Co concentration. It leads to the estimate the orbital contribution: $\chi_p = 9 \times 10^{-5}$ emu/mol for Co^{3+} in $LiCoO_2$. This is of the same order of magnitude as in $NaCoO_2$, but smaller. This difference comes from the fact that χ_p results from a competition between the strength of the crystal field that tends to quench the orbital momentum, and the strength of the spin−orbit coupling that tends to restore an orbital contribution, and the crystal field is not the same in both materials.

The Curie−Weiss contribution is the signature of a magnetic impurity. The Curie constant C gives access to $c\mu_{eff}^2$, where μ_{eff} is the effective magnetic moment of the impurity in concentration c, which is not sufficient to identify the impurity unambiguously. We have already mentioned the presence of Ni. The amount of Ni that has precipitated under the form of Ni nanoparticles that we have determined earlier is smaller than the total amount of Ni that is expected for a cobalt compound, so that part of the Ni is incorporated as a defect in the matrix. In the particular case of $LiCoO_2$, it has been identified by EPR experiments,[40,16] which have shown in addition that the nickel is in the configuration Ni^{3+} in the low-spin state. If we assume that this Ni^{3+} impurity is responsible for the Curie−Weiss behavior, then $\mu_{eff}^2 = 3$, and the value of C deduced from the fit illustrated in Figure 9 leads to a concentration $c = 1.1\%$, which is too high because the Ni^{3+} concentration in cobalt compounds is always smaller than 0.4%. Part of the Curie−Weiss contribution should then have another origin. Most likely, a small concentration of Li vacancies is responsible for it. A concentration c of Li^+ vacancies implies the conversion of the same proportion of Co^{3+} to Co^{4+} configuration to ensure the charge neutrality. We know from earlier studies on Li_xCoO_2 that, in the range $0.95 \le x \le 1$, the Co^{4+} ions are in the high-spin state,[30] so that the Li-vacancy concentration that fits our experimental data is 0.09%, independent of the boron concentration y. The final composition of our samples is then $Li_{0.999}Co_{1-y}B_yO_2$. Yet this Li-vacancy concentration is an overestimation, since it has been derived in the approximation that the contribution of Ni^{3+} impurities to the Curie constant is negligible.

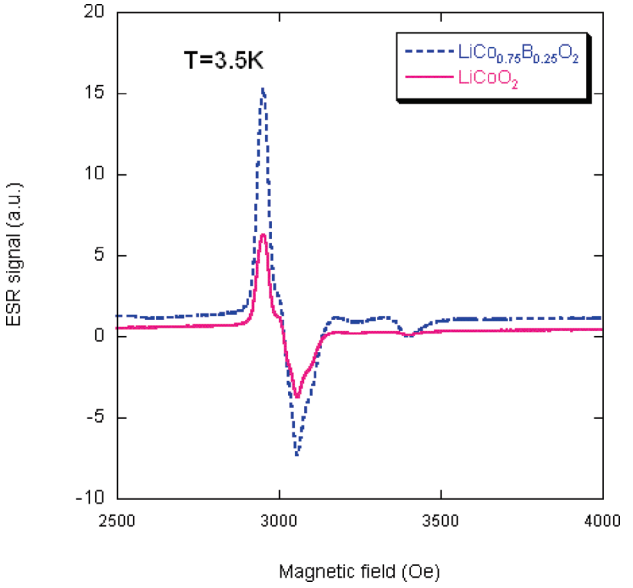

Figure 10. ESR spectra in the high magnetic field region for the $LiCo_{0.25}B_{0.75}O_2$ and a $LiCoO_2$ sample, for comparison.

The paramagnetic Curie temperature is $\theta = 2$ K. This very small value is due to the fact that the concentration of Co^{4+} ions is so small that their magnetic moments do not interact, so that they essentially act as loose spins contributing a Curie law ($\theta = 0$). This simply confirms that the Co^{4+} ions (and thus the Li vacancies) are randomly distributed in the lattice.

3.4. ESR Experiments. ESR experiments are a very sensitive tool to characterize the samples, because the ESR signal scales like the second derivative of the magnetization associated with the Co impurity phase. The result is reported in Figures 10 and 11, for the $y = 0.25$ sample. The result for the undoped sample ($y = 0$) is also reported, for comparison. The units are arbitrary, but are the same in the two figures, so that relative intensities of the signals can be analyzed. The spectrum shows one single signal at 200 G (Figure 11) and signals in the range 2500−3500 Oe (Figure 10), nothing in between. The signal at 200 G is asymmetric. At such a low magnetic field, it cannot be attributed to the ESR resonance on an impurity, since the huge g-factor associated with it would be simply unphysical. This signal is then associated with the alignment of the ferromagnetic particles leading to a sharp increase of the magnetization at this small magnetic field. At larger magnetic field, the thermal fluctuations of the magnetic moment of individual ferromagnetic nanoparticles are frozen. Therefore, at larger magnetic field, these nanoparticles behave like a ferromagnet, and the ferromagnetic resonance (FMR) can be detected. This is

(36) Silinsky, P. S.; Seehra, M. S. *Phys. Rev. B* **1981**, *24*, 419.
(37) Kanamori, J. *Prog. Thor. Phys.* **1956**, *17*, 17. see also Salamon, M. B. *Phys. Rev. B* **1970**, *2*, 214.
(38) Dutta, P.; Seehra, M. S.; Thota, S.; Kumar, J. *J. Phys. C: Condens. Matter* **2008**, *20*, 015218.
(39) Lang, G.; Bobroff, J.; Alloul, H.; Mendels, P.; Blanchard, N.; Collin, G. *Phys. Rev. B* **2005**, *72*, 094404.
(40) Angelov, S.; Friebel, C.; Zhecheva, E.; Stoyanova, R. *J. Phys. Chem. Solids* **1992**, *53*, 443.

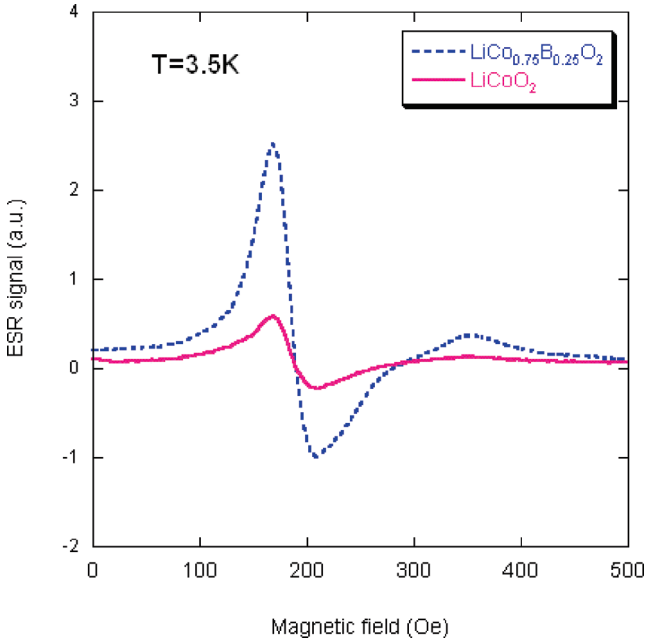

Figure 11. ESR spectra in the low magnetic field region for the $LiCo_{0.25}B_{0.75}O_2$ and a $LiCoO_2$ sample, for comparison.

the signal centered at 3000 G in Figure 10, which corresponds to the gyromagnetic factor $g = 2.20$, characteristic of the FMR resonance of nickel particles.[41,42] Of course, the amount of nickel may vary form one sample to another, hence the difference in amplitude of the signal between the two samples; however, the relative intensities between the signal centered at 200 Oe and the signal centered at 3000 G are the same for both samples, so that they associated with the same impurity. This is the confirmation that the signal at 200 G is due to the alignment of the individual moments of the Ni nanoparticles, the FMR signal of which is the signal centered at 3000 Oe. It is evident from Figure 10 that another signal is superimposed to the signal at 3000 G. To deconvolute the two signals, we have integrated the ESR signal, to obtain the absorption spectrum reported in Figure 12 for the $LiCo_{0.75}B_{0.25}O_2$ sample. Standard routines used for the deconvolution of infrared of Raman spectra are then used to deconvolute this absorption spectrum. We found this procedure much more convenient than working on the ESR signal itself. In particular, we found it impossible to fit the ESR signal as a superposition of two resonances of Lorentzian shape. Instead, the result of the deconvolution of the absorption signal, also shown in Figure 11, shows that the signal is the superposition of two resonances of Gaussian profile, the one centered at 3000 Oe already discussed, the other centered at 3080 G. This field corresponds to a gyromagnetic factor $g = 2.14$, which is the signature of low-spin Ni^{3+} ions substituted isomorphically to the Co^{3+} ions.[40,16] The Gaussian profile, rather

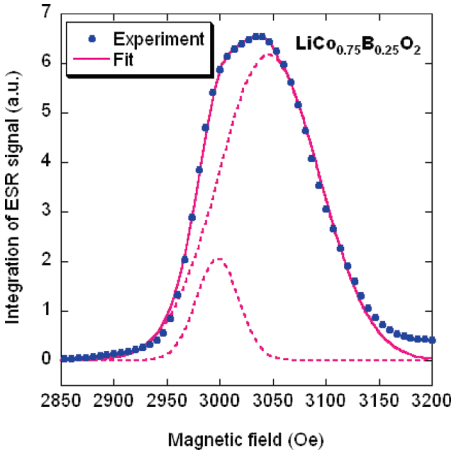

Figure 12. Integrated ESR signal and deconvolution in two absorption peaks of Gaussian profile (broken curves) for the $LiCo_{0.25}B_{0.75}O_2$ sample. Dots are experimental data (10% of the data only have been reported for clarity). The full curve is the fit of the data (sum of the two Gaussians).

the Lorentzian profile is indeed expected for the Ni^{3+}, which is a Jahn−Teller ion sensitive to random anisotropy associated with local strains. In the case of metallic nickel, the Gaussian profile of the resonance at 3000G is more likely due to the long-range dipolar interaction between the magnetic moments of the Ni particles.

The same analysis is illustrated in Figure 13 for a $LiCoO_2$ (undoped) sample for comparison. The intensities of the signals at 3000 and 3080 Oe have the same order of magnitude, as expected, because Ni impurity is introduced by the cobalt precursor. However, the relative intensities between the two deconvoluted peaks are not identical, which means that the fraction of nickel that has segregated with respect to the nickel ions diluted in the matrix are not the same in the two samples. However, it is not possible at this stage to determine if this difference is just a statistical fluctuation inherent to any extrinsic effect, or if it is related to the boron in one of the sample. To answer this question, similar measurements should be performed on many samples, which is not the purpose of the present work.

Finally, another signal centered near 3300 G ($g = 2$) in the B-doped samples is attributable to the presence of Co^{4+} ions detected by the magnetic measurements, since this ion is in a pure spin state $S = 5/2$ (no orbital momentum).

3.5. Electrochemical Studies. The charge−discharge profiles of $Li//LiCo_{1-y}B_yO_2$ cells using boron-doped lithium cobaltates were investigated at rate $C/4$ with various levels of B substitution ($0.05 \leq y \leq 0.35$). Figure 14 shows the first charge−discharge curves for $Li//LiCo_{1-y}B_yO_2$ cells operated between 2.5 and 4.4 V. The open-circuit voltages of freshly assembled cells were 2.8 to 3.0 V. At the cutoff voltage of 4.4 V, the gravimetric capacity of the $Li//LiCo_{0.95}B_{0.05}O_2$ cell is ca. 140 mA h/g at the end of the first discharge (3.0 V), which is a value similar to that delivered by $LiCoO_2$ cathode. On another hand, the capacity decreases significantly for cathode materials $LiCo_{1-y}B_yO_2$ with $y = 0.20$. A specific gravimetric capacity of 118 mA h/g was obtained for a $Li//LiCo_{0.65}B_{0.35}O_2$ cell. This decrease in capacity when y increases was indeed expected, because the boron ion remains in the B^{3+}

(41) Vergand, F.; Fargues, D.; Oliver, D.; Bonneviot, L.; Che, M. *J. Phys. Chem.* **1983**, *87*, 2373.
(42) Isupov, V. P.; Tarasov, K. A.; Chupakhina, L. E.; Mitrofanova, R. P.; Starikova, E. V.; Yulikov, M. M.; Mart'yanov, O. N.; Yudanov, V. F.; Ermakov, A. E.; Andreeva, O. B. *Dokl. Chem.* **2003**, *391*, 200.

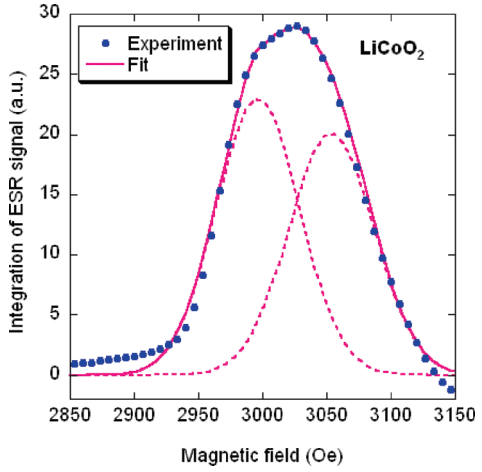

Figure 13. Same as Figure 10 for $LiCoO_2$ for comparison.

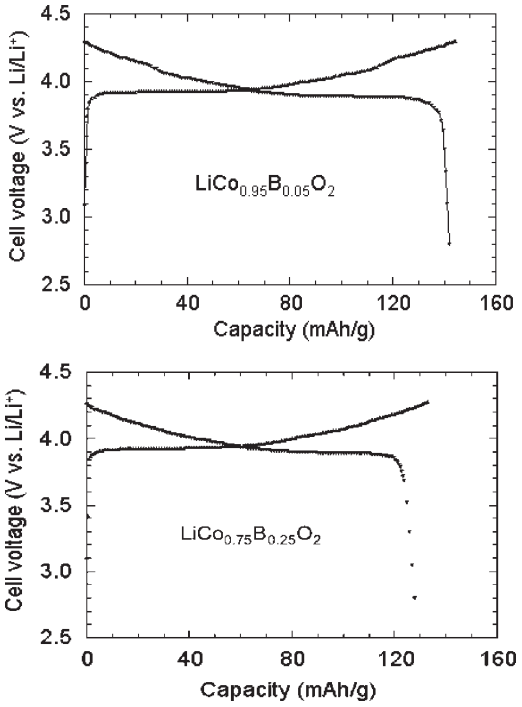

Figure 14. Charge−discharge profiles of $Li//LiCo_{1-y}B_yO_2$ cells using lithium cobaltates with various levels of B substitution ($y = 0.05$ and 0.25,), at rate $C/4$.

trivalent state and thus does not participate in the lithiation/delithiation process.

The cells containing $LiCo_{1-y}B_yO_2$ positive electrodes were on average 80% efficient when compared to their expected theoretical capacities (in theory, the fully charge state is defined as the configuration where Li ions cannot be extracted from the host matrix because no electrons are removed from either B^{3+} or Co^{4+} and all the Co^{3+} have been converted in Co^{4+} ions). The deintercalation of Li^+ ions in $Li_xCo_{0.75}B_{0.25}O_2$ ends around $x = 0.45$ (Figure 14); thus the corresponding reaction is

$$[Li_{0.45}]_{3a}[Co^{4+}{}_{0.55}Co^{3+}{}_{0.20}B^{3+}{}_{0.25}]_{3b}[O_2]_{6c} + 0.55Li^+ + 0.55e^- \leftrightarrow [Li]_{3a}[Co_{0.75}B_{0.25}]_{3b}[O_2]_{6c} \quad (4)$$

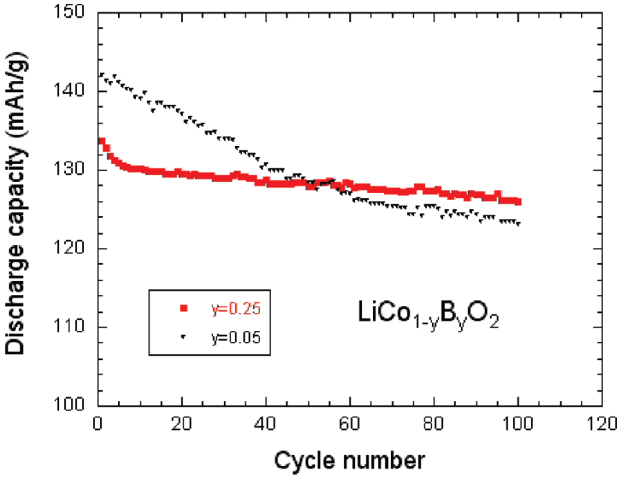

Figure 15. Capacity fading of $Li//LiCo_{1-y}B_yO_2$ cells using lithium cobaltates with two levels of B substitution.

On another hand, the recharge ability of the $Li//LiCo_{1-y}B_yO_2$ cells seems better than $LiCoO_2$ because the lack of the two-phase behavior in the high-voltage region. During the first discharge, about 10 mA h/g is irreversibly lost. Figure 15 shows the capacity fading of $Li//LiCo_{1-y}B_yO_2$ cells using lithium cobaltates with various levels of B substitution. It illustrates that irreversibility during the first cycle is a less severe problem in the case of B-substituted lithium cobaltates. High reversibility with low overpotential polarization was observed during charge−discharge cycles of the $LiCoO_2$ doped with B. Sample of $LiCoO_2$ with 15% B substitution provides 139 mA h/g, when charged up to 4.4 V vs metallic Li anode. $LiCo_{0.75}Al_{0.25}O_2$ provides a gravimetric capacity of 127 mA h/g at the end of the first discharge when charged up to 4.4 V. The charge and discharge profiles are fairly monotonous, indicating that no structural transition occurred.

4. Discussion

The results showed that the cell using the $LiCo_{0.75}B_{0.25}O_2$ compound performed slightly better than the other ones; the gravimetric capacity remains almost unchanged up to the 16th cycle, and the aging was found very small upon cycling at $C/4$, as shown in Figure 15. This indicates that for B^{3+} incorporation, the optimum dopant level for gravimetric capacity and life cycle ability would be approximately $y = 0.25$.

This performance is partly due to the quality of the sample. $LiCoO_2$ is usually poisoned by impurities that are evidenced by an anomaly in the magnetic susceptibility at 160 K, which is more or less pronounced, depending on the sample quality.[30] In the present case, no such anomaly has been detected (see Figures 8 and 9). Magnetic properties are the best tool to characterize the material, provided a distinction is made between impurity effects and intrinsic properties. In particular, a magnetic transition at $T \approx 50$ K with a transition width 30 K has been considered as an intrinsic property in a prior work, and tentatively attributed to a disproportionation $2Co^{3+} \rightarrow Co^{2+} + Co^{4+}$.[43] This is impossible, and actually not observed,

because such a disproportionation would generate a magnetic susceptibility 3 orders of magnitude larger than the experimental value $\chi(T)$ observed in the present work and the prior works including ref [43] as well. The opposite is true, i.e., there is a single nonmagnetic Co^{3+} state in $LiCoO_2$, which also means that, contrary to the claim in,[43] this material is not a realization of a frustrated antiferromagnetic triangular lattice. The presence of Co^{4+} in our samples in very small concentration (0.09%) is attributable to lithium vacancies, and of course this concentration is independent of the temperature, as it is shown by the fit of the magnetic susceptibility at all temperatures. Note that this property is a general property of cobaltates, because it also applies to $NaCoO_2$ for instance.[39] We believe that the magnetic ordering in[43] is the signature of Co_3O_4 used as a precursor, which still remains as nanostructured impurity phase in the sample of ref 43. Indeed, bulk Co_3O_4 orders antiferromagnetically at 40 K, and the ordering temperature of nanoparticles of Co_3O_4 depends on the size of particles, hence the width of the transition that has been observed.

The sample quality, however, is not sufficient to explain the electrochemical performance and is also linked to the following effect. "Pure" Li_xCoO_2 is known to undergo a first-order structural transition from hexagonal to monoclinic phase at $x = 1/2$. This is due to an orbital ordering or equivalently a cooperative Jahn−Teller effect. For this reason, we shall call it for simplicity JT transition. Whether or not this structural transition is also a charge ordering transition (Verwey-type transition) is a debate that has been addressed in $LiMn_2O_4$ in ref 44. In any case, the onset of a periodic alternate arrangement of these two charges or the cooperative distortion that generates the structural transition require the same amount of Co^{3+} and Co^{4+} in the lattice, the reason why it is observed at the composition $x = 1/2$. It also means that this first-order transition is very sensitive to any defect, and even a small concentration of defects is usually sufficient to prevent it. This sensitivity is even of practical interest; for instance, the observation or not of this transition in $LiMn_2O_4$ is a criterion for the purity of the samples.[45] The boron dopant in Li_xCoO_2 is a defect. In particular, boron will remain trivalent upon delithiation, thus preventing the formation of a Li vacancy in its vicinity that would require a tetravalent state to maintain charge neutrality. Therefore, Boron opposes the ordering of Li vacancies, and as such it opposes the first-order transition to the monoclinic phase associated with this charge ordering. This is evidenced in Figure 16, where we have reported the intensity versus voltage curve under the same operating conditions as in Figure 14 (first cycle, charge rate $C/4$). We find the well-known main oxidation peak ca. 4 V, just like in the case $y = 0$ where it has been attributed to the

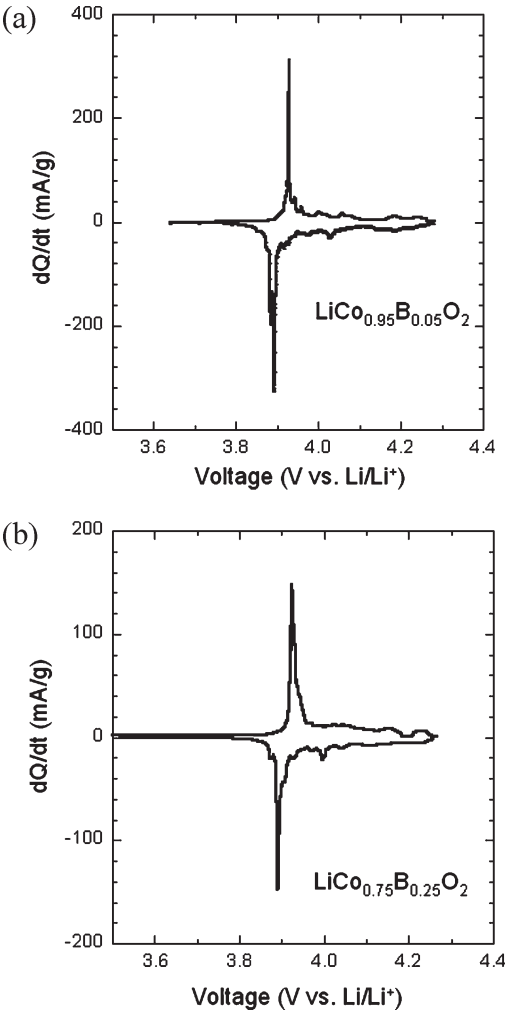

Figure 16. Intensity versus voltage curve under the same operating conditions as in Figure 12 (first cycle, charge rate $C/4$).

transition from $LiCoO_2$ to $Li_{0.8}CoO_2$ accompanied by an expansion of the c-hexagonal lattice parameter.[10,46] In the case $y = 0.05$, a small secondary maximum at 4.1 V is also observed in Figure 16. It has been identified in the case $y = 0$ to the structural Verwey-type or JT-driven transition of $Li_{0.5}CoO_2$. This transition is then still observed for this small boron concentration. On another hand, it has disappeared in samples with larger boron concentration $0.05 < y \leq 0.25$, which gives evidence that the concentration of B_{Co} defects is now large enough to suppress the Verwey transition. The same effect is actually observed in case the impurity is nickel instead of boron.[46] As a consequence, the lattice does not have to adjust the lattice distortion associated with the cooperative charge ordering effect at each lithiation/delithiation cycle, hence an improved cyclability. In addition, it makes possible the delithiation of the material down to $x = 0.45$, after eq 2, whereas the extraction is limited to $x = 0.5$ in "pure" $LiCoO_2$ because of the Verwey transition. On another hand, we have shown in this work that larger boron concentrations exceed the limit of solubility of born in

(43) Sujiyama, J.; Nozaki, H.; Brewer, J. H.; Ansaldo, E. J.; Morris, G. D.; Delmas, C. *Phys. Rev. B* **2005**, *72*, 144424.This article has also been published in Physica B **2006**, *374*, 148.
(44) Grechnev, G. E.; Ahuja, R.; Johansson, B.; Erickson, O. *Phys. Rev. B* **2002**, *65*, 174408.
(45) Kopec, M.; Dygas, J. R.; Krok, F.; Mauger, A.; Gendron, F.; Julien, C. M. *J. Phys. Chem. Solids* **2008**, *69*, 955.
(46) Reimers, J. N.; Dahn, J. R.; von Sacken, U. *J. Electrochem. Soc.* **1993**, *140*, 2752.

this material, which implies that part of the boron will then precipitate to form amorphous pyroborate and/or metaborate clusters. That is the reason why the Verwey transition is recovered in the $y = 0.35$ sample, implying a plastic deformation of the lattice upon cycling resulting in a loss of capacity. This is in essence the reason why the optimum dopant level for gravimetric capacity and life cycle ability is the limit of solubility, the order of $y = 0.25$. This solubility limit in the $LiCo_{1-y}B_yO_2$ cathode materials is in good agreement with the work of Nazri et al.[17]

The theoretical capacity of "pure" $LiCoO_2$ is 274 mA h/g. However, because of the Verwey transition abovementioned, it is impossible in practice to extract more than half of the lithium in a reversible manner, so that the capacity available for "pure" $LiCoO_2$ is 137 mA h/g only. For the boron-doped sample at $y = 0.25$, we have obtained a capacity 130 mA h/g that is almost unchanged in the same potential window $V \leq 4.4$ V imposed for safety of the electrolyte. In addition, while "pure" $LiCoO_2$ has to be protected against overcharge, the boron-doped cathode does not need such a protection, since the Verwey transition is avoided. Indeed, more stable charge−discharge cycling performances have been observed as compared to the performances of the native oxides, even when 0.55 Li per mole is extracted during the charge, according to eq 2. Less than 10% capacity fading was observed at the end of few ten deep charge−discharge cycles performed between 2.8 and 4.4 V.

As discussed above, there are similarities between the Verwey transitions in Li_xCoO_2 and Li_xNiO_2 at $x = 0.5$. There are, however, differences too. In-plane ordering of lithium and vacancies implies a structural change in the lattice that can be modified by varying the ratio a/b of the lattice parameters and/or the angle β. The changes are, however, very different in both materials. Changes in the a/b ratio would modify the cobalt−oxygen bonds and distort the CoO_6 octahedra, which is energetically unfavorable since both Co^{3+} and Co^{4+} prefer to occupy ideal or nearly ideal octahedral sites. That is why the $Li_{0.5}CoO_2$ adopts a negligible change in the a/b ratio (1.733), but a significantly different β (107.89°).[47] In contrast, $Li_{0.5}NiO_2$ adopts a small change in β, but a large increase of a/b, because Jahn−Teller distorted Ni^{3+} can accommodate the lattice distortion in the a and b directions. This feature also explains that the lattice parameters do not significantly depend on the boron concentration in $LiCoO_2$, despite the difference in the ionic radii between cobalt and boron. We know from optical spectroscopy data that boron in the coplanes, and thus, for symmetry reasons in substitution to cobalt. This rigidity of the lattice imposed by the need to keep the octahedral environment of cobalt leads to the picture of a boron ion "rattling" in the rigid cage formed by the CoO_6 octahedra. The vibrations associated with this rattling are very low frequency modes that cannot be observed in the frequency range we have explored in FTIR and Raman experiments, which is consistent with the lack of any vibration associated with B−O vibrations in Raman spectra, in the limit of solubility of boron, i.e., when boron is in substitution to cobalt.

(47) *Lithium Batteries: Science and Technology*; Nazri, G., Pistoia, G., Eds.; Springer: New York, 2004.

5. Conclusion

These studies have shown that the layered structure of boron-substituted $LiCo_{1-y}B_yO_2$ materials is preserved upon a large amount of B incorporation ($y \leq 0.25$), for which no residual impurity phases were detected. An overall understanding of all the structural, chemical and electrochemical properties has been achieved. The limit of solubility of boron is the order of $y = 0.25$, which is also the composition that optimizes the electrochemical properties. The experimental gravimetric capacity of the $Li//LiCo_{1-y}B_yO_2$ system is almost independent of y up for $y \leq 0.2$, but the boron-doping improves importantly the cycling performance of the battery, as the boron impurity favors lattice adaptation to the insertion/extraction of lithium, and prevents the onset of the structural first-order transition associated with the Verwey transition in $Li_{0.5}CoO_2$.